Online-Journals.org

iJOE International Journal of Online and Biomedical Engineering

iJOE | eISSN: 2626-8493 | Vol. 22 No. 3 (2026) | OPEN ACCESS

https://doi.org/10.3991/ijoe.v22i03.59151

PAPER

An IoT Device for Monitoring the Respiratory Rate of People in Motion

Jhosep Ccoanqui, Eros Huamani, Guillermo Kemper (✉)

Universidad Peruana de Ciencias Aplicadas, Lima, Peru

guillermo.kemper@upc.pe

ABSTRACT

This work presents the development of a wireless Internet of Things (IoT) device that continuously monitors the respiratory rate (RR) of a person in motion. Unlike existing solutions, whose sensors are adversely affected by perspiration and exhibit low accuracy at high velocities, the proposed IoT device integrates a triaxial magnetic sensor that measures changes in the magnetic field due to chest movement, using the Z-axis information to estimate respiratory rate. The developed device uses an IIR Butterworth low-pass filter and a peak detection algorithm to overcome noise inherent to user motion and accurately extract the respiratory signal. It incorporates dual communication (Bluetooth for local connection and WiFi for cloud transmission), ensuring highly reliable real-time data transmission. System validation consisted of measuring the percentage error in 10 volunteers under three scenarios (rest, normal motion, and accelerated motion). The results demonstrate an accuracy greater than 95% in estimating respiratory rate, achieving an average percentage error of 2.36% at rest, 2.32% during normal motion, and 1.61% during accelerated motion.

KEYWORDS

respiratory rate, Internet of Things (IoT), monitoring, motion

1 INTRODUCTION

The monitoring of respiratory rate (RR) is widely used in medical assessments, from the diagnosis and monitoring of chronic respiratory diseases to the early detection of adverse events in clinical and home settings [1]. In recent years, technological advancements have driven the development of portable and wireless devices that facilitate monitoring outside of clinics or hospitals. However, despite these advances, the implementation of respiratory monitoring systems during motion conditions continues to present challenges.

Among current solutions, one uses a microphone to estimate respiratory rate; however, it requires acoustic isolation to avoid interference from environmental

Ccoanqui, J., Huamani, E., Kemper, G. (2026). An IoT Device for Monitoring the Respiratory Rate of People in Motion. *International Journal of Online and Biomedical Engineering (iJOE)*, 22(3), pp. 94–113. https://doi.org/10.3991/ijoe.v22i03.59151

Article submitted 2025-10-12. Revision uploaded 2025-12-14. Final acceptance 2025-12-14.

noise, such as the use of a mask [2]. Likewise, solutions based on sensors sensitive to humidity, such as those measuring skin impedance or conductivity, are prone to errors in the presence of perspiration—a common factor during physical activity [3]. Furthermore, most of these devices demonstrate limited accuracy at high movement velocities, such as those observed in sports activities or dynamic daily life, where motion artefact significantly contaminates the respiratory signal [4]. These deficiencies restrict the reliability and usefulness of such technologies in scenarios where uninterrupted and accurate monitoring during movement is critical, such as in tracking athletes, patients with respiratory conditions who maintain an active lifestyle, or telemedicine applications requiring robust real-time data [1].

Consequently, recent research has investigated emerging technologies to overcome these limitations, including printed flexible sensors [5], advanced materials for piezoresistive detection [6], and intelligent systems integrated into textiles with regulatory approval [7]. In addition, commercial solutions such as RTMsense incorporate artificial intelligence algorithms to enhance accuracy and provide predictive analytics [8]. Altogether, these trends reflect a shift toward robust IoT devices that combine connectivity, digital processing, and interference resistance, establishing a new paradigm in respiratory monitoring [9].

Building on these advances, this proposed work presents the development of an innovative wireless IoT device specifically designed for monitoring during movement. It addresses the limitations of existing technologies by integrating a triaxial magnetic sensor. This type of sensor offers an advantage by measuring changes in the magnetic field generated by chest movement, making it less susceptible to interference from perspiration. Furthermore, the system implements a signal processing algorithm, which includes an IIR Butterworth low-pass filter with a cutoff frequency of 0.5 Hz and a peak detection method, optimised to discriminate motion noise and accurately extract the respiratory signal. The device also incorporates a dual communication architecture (Bluetooth and WiFi), ensuring real-time data transmission both locally and to cloud platforms using MQTT technology. Through this work, the authors aim to establish a new standard for the accuracy and reliability of respiratory monitoring in dynamic environments, offering a tool for healthcare professionals, researchers, and end-users who require precise physiological data without the constraints imposed by movement.

2 RELATED WORK

Table 1 presents previous works, along with their strengths and weaknesses.

Table 1. Solutions and proposals in the state of the art

Reference	Technique	Application	Strengths	Weaknesses	Proposed Device
[4]	A stretchable strain sensor integrated into a wearable system.	Monitoring of RR during moderate exercise.	Provides portable, comfortable, and accurate monitoring of RR during moderate exercise thanks to its sensor.	Sensitivity to sudden movements or perspiration, limitations during high-intensity exercise, and dependence on calibration and optimal skin contact.	Its functionality is not affected by high-intensity exercise.

(Continued)

Table 1. Solutions and proposals in the state of the art *(Continued)*

Reference	Technique	Application	Strengths	Weaknesses	Proposed Device
[3]	Wireless wearable ultrasound-based sensor designed for continuous monitoring of respiratory behaviour.	To continuously monitor respiratory behaviour and deliver clinically relevant respiratory information to a smartphone.	The sensor is lightweight and compact, facilitating prolonged use. Applicability in asthma control, enabling constant monitoring and alerting the patient when lung function values indicate inflammation or deterioration.	Limited to monitoring people moving at speeds of up to 7.2 km/h. Uses only a Bluetooth module. Uses substrate paper adhered to the skin, which during prolonged exercise may reduce its performance upon contact with sweat.	Its high sensitivity allows it to be used in situations of intense exercise.
[10]	Wearable chest patch based on bioimpedance (BioZ), integrated with a medical-grade infrared temperature sensor and wireless communication protocols (Bluetooth and LoRa).	Continuous ambulatory respiratory monitoring during static and dynamic activities, with the capability to detect RR and correlate physiological data with physical activity.	Combines high accuracy in static and dynamic respiratory monitoring, multimodal integration, extended portability (12 h), and resistance to motion artefact interference.	Depends on optimal skin contact, limiting its use during intense exercise or excessive perspiration.	The sensor used has no direct contact with the user's skin.

As detailed in Table 1, systems reported in the literature present critical limitations, including sensitivity to sudden movements and perspiration, restriction to speeds below 7.2 km/h, dependence on calibration and optimal skin contact, as well as the absence of remote monitoring capabilities. To address these deficiencies, this work presents a comprehensive solution based on a robust signal acquisition and processing architecture.

The fundamental contribution is underpinned by the GY-271 QMC5883L magnetometer, selected for its technical advantages: an I^2C digital interface that eliminates analogue interference, a measurement range of ±8 Gauss providing robustness against abrupt variations, and a 16-bit ADC that guarantees high resolution in capturing the variations of the respiratory magnetic field. This choice directly overcomes the reported state-of-the-art limitations regarding sensitivity to motion and perspiration.

The signal processing implements a fifth-order low-pass Butterworth filter (0.5 Hz) that efficiently suppresses high-frequency noise and motion artefacts while preserving the fundamental respiratory morphology. On this filtered signal, a peak detection algorithm identifies the local maxima corresponding to each inhalation, calculating the RR from the temporal interval between peaks with an accuracy greater than 95%.

The proposed IoT device demonstrated a relative error below 5% during high-intensity running (>8 km/h), surpassing the main speed limitation of the state of the art and validating its efficacy under intense exercise conditions where conventional systems fail.

In addition to the reduced relative error, the technological contributions include:

- A dual transmission architecture (Bluetooth + Wi-Fi) enabling both local monitoring and remote data sending to cloud platforms.
- An energy management system with an LED battery indicator that prevents critical failures.
- Validation under realistic conditions of intense exercise, overcoming the limitations of conventional systems.

The following sections describe the wearable device, the algorithms, and the corresponding results.

3 MATERIALS AND METHODS

This section details the materials and methods applied in both the hardware aspect (electronics and device structure) and the software aspect (signal processing and peak detection algorithms). The selected materials and methods are the result of a selection process that considered various experimental tests, application scenarios, user experience and transport, energy autonomy, computational efficiency, and engineering fundamentals.

3.1 Materials

The development of the respiratory monitoring device is based on the selection of components that provide precision, connectivity, and energy efficiency.

The core module is the NodeMCU-32 30-PIN ESP32 WIFI, previously used in several biomedical applications such as abdominal force monitoring via EMG and real-time transmission [11], supporting its selection for this work. It integrates a dual-core CPU with 2.4 GHz Wi-Fi and Bluetooth v4.2 Low Energy (BLE) capabilities [12]. This connectivity duality enables both local communication with mobile devices via Bluetooth and data transmission to the cloud via Wi-Fi. Furthermore, the ESP32 offers a wide range of peripherals (UART, I2S, I2C), facilitating connection with the sensors and other necessary components.

The sensor for magnetic field detection is the GY-271 QMC5883L. It was selected for its I^2C digital interface, a measurement range of ±8 Gauss, and an integrated 16-bit analogue-to-digital converter (ADC) [13], enabling accurate reading of the magnetic field variations generated by chest movement.

The monitor for the battery state of charge is the MAX17043. It utilises the ModelGauge™ algorithm for Li+ (lithium-ion) batteries [14], allowing the user to track the available charge percentage in real time.

Finally, for circuit protection and user safety, the XC6220B331MR low-dropout (LDO) regulator is used against overcurrent (OCP) and overtemperature (TSD), preventing critical damage to the device [15]. Likewise, an SMD LED indicator provides a clear visual signal of the battery level.

These components work together to provide a reliable and safe respiratory monitoring solution during movement.

3.2 Methods

This section describes the methodology implemented for the development and validation of the IoT respiratory monitoring device. The study is organised into three main stages: (1) physiological signal acquisition and conditioning, (2) digital data processing and filtering, and (3) peak detection and RR estimation. Each phase was meticulously designed to ensure accuracy in the capture, processing,

and interpretation of respiratory signals, utilising specialised electronic components and digital signal processing (DSP) algorithms.

Structure and electronics of the proposed IoT device. The schematic of the proposed IoT device is shown in Figure 1.

The system consists of the ESP32 programming circuit, which acts as a bridge between the computer and the microcontroller, as seen in Figure 1. This circuit includes a UART connector (J2) with TXD0 (transmit), RXD0 (receive), and GND lines for serial communication. Two buttons serve critical functions: S1 generates a reset by connecting the RESET pin to ground via an RC circuit (R1/C4), while S2 forces the GPIO0 pin to GND (using R2/C5) to activate programming mode.

The system's core component is the ESP32-WROOM-32 System-on-a-Chip (SoC) [12], which processes data from the magnetometer. Its stability depends on a capacitor on the power supply input (VDD); the absence of this capacitor would cause random reboots, interference, or damage from voltage fluctuations. This SoC communicates with the sensor via the I^2C protocol through its SDA and SCL pins (see Figure 1).

The QMC5883L sensor is responsible for measuring magnetic fields. Its internal architecture uses three AMR (anisotropic magnetoresistance) bridges (for X/Y/Z axes) that detect resistance changes under magnetic fields. A multiplexer (MUX) selects each axis, followed by a Programmable Gain Amplifier (PGA) and an ADC that digitises the signals. Thermal compensation circuits, a clock generator (CLK Gen), and SET/RESET functions ensure accuracy [13]. It communicates with the ESP32 via I^2C, using 10 kΩ pull-up resistors (R3/R4) on SDA/SCL, while a capacitor bank (C7-C10) filters noise on its 3.3 V power supply (see Figure 1).

Power management is handled by a regulator (XC6220B331MR) that converts the 3.7V from a 1000mAh battery to a stable 3.3V output [15]. TSD Protection (OTP) devices (OTP1/OTP2) protect against overheating, and electrolytic capacitors (C2/C3) stabilise the output. The battery gauge (MAX17043) monitors the voltage via a resistive divider (R5) (see Figure 1), calculates the state of charge, and alerts with the ALERT pin if the level is critical, communicating data to the ESP32 via I^2C [14].

A 1000 mAh, 3.7 V lithium battery is used to ensure an autonomy exceeding 8 hours. The device's operational current consumption is 87 mA, resulting in an operational time of ~11.5 hours. This performance meets the required autonomy target.

Finally, three RGB LEDs connect to the ESP32's GPIO12 (red), GPIO13 (green), and GPIO14 (blue) pins—each with its current-limiting resistor (See Figure 1)—providing visual feedback on the battery status, thereby closing the loop of an integrated system that autonomously captures, processes, and displays data.

The design of the proposed IoT device required the development of the printed circuit board (PCB) and its protective casing. This casing, with dimensions of 56.2 mm (length) × 39.4 mm (width) × 18 mm (height), was modelled to securely house the PCB and protect all electronic components. Finally, an adjustable Velcro strap (5 cm × 125 cm) is integrated to the device assembly to facilitate chest attachment. The final design of the proposed IoT device is shown in Figure 2.

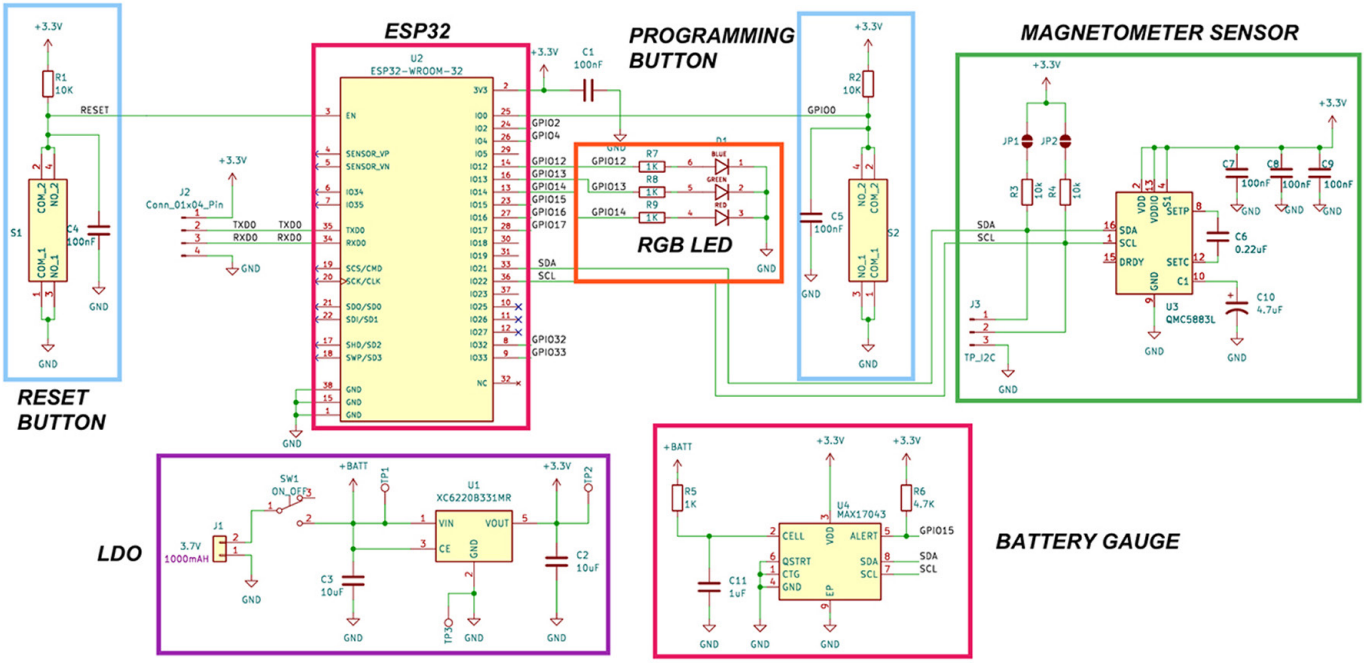

Fig. 1. Schematic of the proposed IoT device

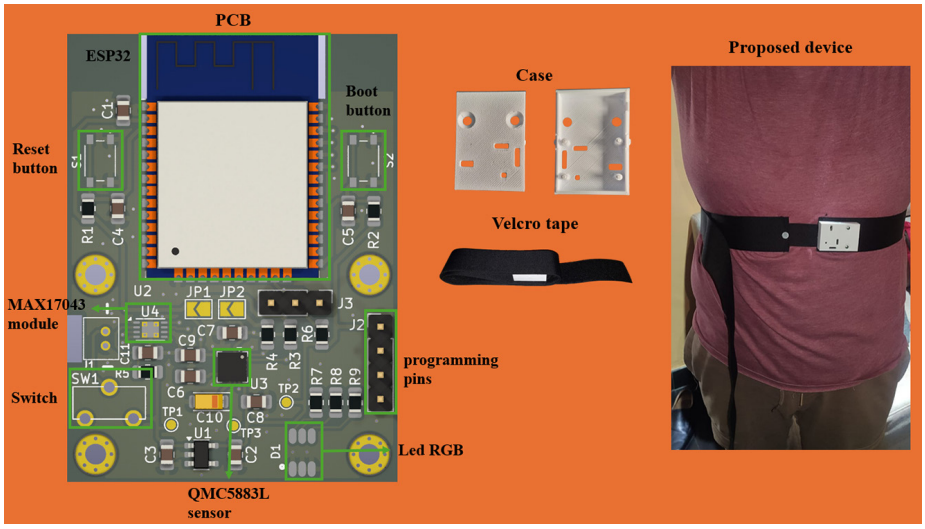

Fig. 2. Device structure

Signal acquisition of respiration. The diagram in Figure 3 describes the signal conditioning process, which begins with the digitisation of analogue magnetic field readings along the three axes via an ADC. These signals are segmented into blocks, and the mean value is subsequently subtracted to centre the signal at the origin.

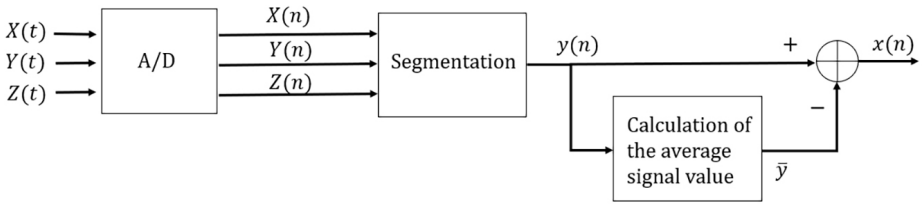

Fig. 3. Signal acquisition and processing diagram

The following digitisation parameters were configured to read sensor data via I2C serial communication: a sampling frequency f_s of 10 Hz and a resolution of 16 bits per sample, corresponding to the integrated ADC of the sensor. The choice of sampling frequency is justified since the maximum normal RR of an adult during movement is 40 breaths per minute [16] (0.67 Hz), and the selection of bit depth per sample is based on the approximately 14,000 G magnetic field of the neodymium magnet [17].

To obtain the magnetic field axes, the read method from the MechaQMC5883 library is used. The data are transmitted to a PC or mobile device via Bluetooth or Wi-Fi for processing. The magnetic field is read over a user-defined block time T_B as shown in Equation 1.

$$\begin{gathered} y(n) = k\,(n + bN) \\ n = 0, 1, 2, \ldots, N-1 \\ b = 0, 1, 2, \ldots \\ N = f_s \times T_B \end{gathered} \tag{1}$$

Where:

- $y(n)$: Sampled signal
- k: Original signal
- b: Block number
- N: Block size
- f_s: Sampling frequency
- T_B: Block time

Signal analysis revealed that while all three axes register information about chest deformation, the Z-axis provides the clearest signal with the most informative content relevant to respiration, as shown in Figure 4. The X and Y axes, shown in Figures 4a and 4b respectively, although containing data, exhibit higher levels of noise and artefacts, making them less suitable for processing. This clear superiority in the signal quality of the Z-axis, demonstrated in Figure 4c, motivated its selection as the signal of interest for subsequent analysis.

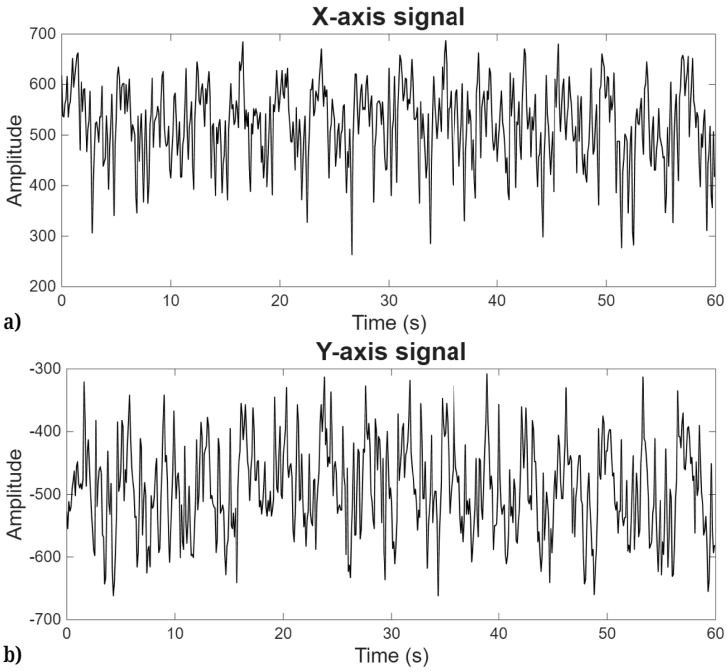

Fig. 4. *(Continued)*

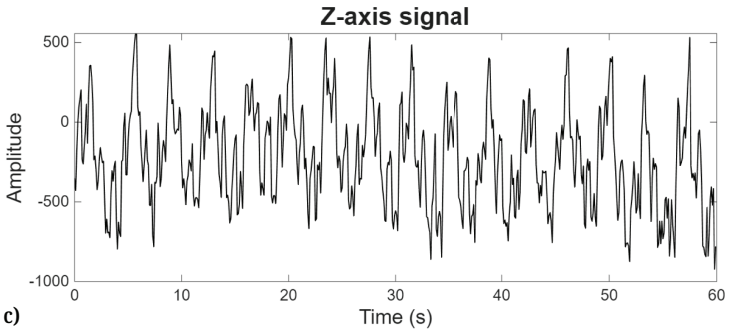

Fig. 4. Original signal across the three axes: (a) x-axis, (b) y-axis, (c) z-axis

The mean value of the signal is subtracted from the original signal to eliminate the DC component, thereby centring the signal at the origin, as shown in Equations 2 and 3.

$$\bar{y} = \frac{1}{N}\sum_{n=0}^{N-1} y(n) \tag{2}$$

Where:

- $\bar{y}$: Mean value of the signal
- N: Block size
- $y(n)$: Original signal

$$x(n) = y(n) - \bar{y} \tag{3}$$

Where:

- $x(n)$: Centred signal
- $y(n)$: Original signal
- $\bar{y}$: Mean value of the signal

Noise and distortion reduction. The diagram illustrates the implementation of a bidirectionally applied low-pass Butterworth filter, which effectively eliminates high-frequency noise from the respiratory signal while preserving its original phase. This processing yields a clean signal that facilitates accurate identification of respiratory cycles, as shown in Figure 5.

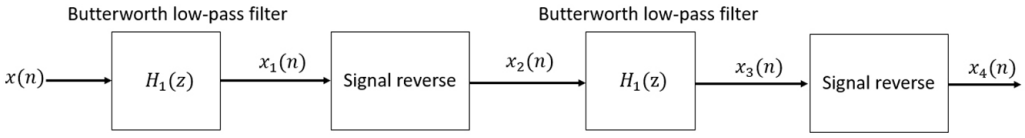

Fig. 5. Signal processing diagram

To eliminate signal noise, a fifth-order low-pass Butterworth filter with a cutoff frequency of 0.5 Hz was used, as employed in [16]. The choice of cutoff frequency is justified by the average duration of one breath per second in humans [16]. The frequency response was evaluated using Bode plots, as shown in Figure 6. The fifth-order filter exhibits a steeper transition between the passband and stopband, significantly reducing spectral energy outside the respiratory range and enabling more effective suppression of high-frequency components generated by non-respiratory movements.

The fifth-order Butterworth filter provides the best performance in cleaning the original signal contaminated by motion artefacts. This is consistent with its frequency response: Figure 6a shows a steeper attenuation at frequencies above the cutoff, thereby more aggressively eliminating noise. Although this characteristic introduces greater phase distortion, as shown in Figure 6b, the net result is a filtered signal where the component of interest is preserved with greater clarity compared to lower-order filters, as observed in Figure 7. Figure 7a displays the original contaminated signal. However, applying the 3rd- and 4th-order filters still reveals undesired peaks, as seen in Figures 7b and 7c. Consequently, applying the 5th-order filter eliminates these undesired peaks, as shown in Figure 7d.

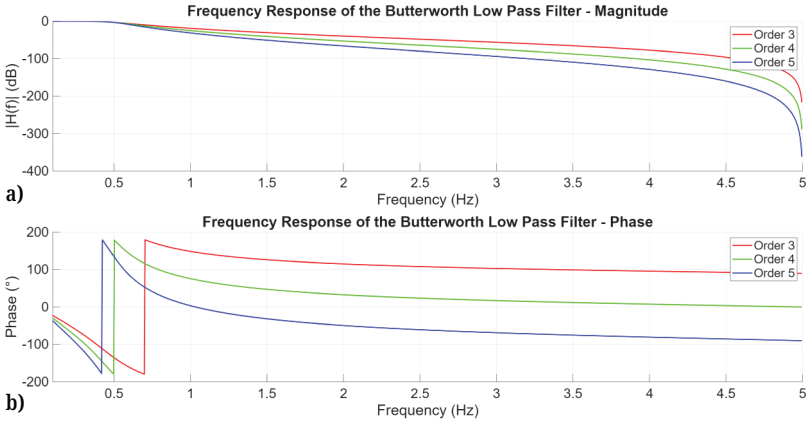

Fig. 6. Bode plot of the 3rd, 4th, and 5th order low-pass Butterworth filter: (a) frequency response – magnitude, (b) frequency response – phase

Equation 4 shows the system function of the 5th-order digital low-pass Butterworth filter, which yielded the best results. The values of its coefficients are presented in Tables 2 and 3.

$$H_1(z) = \frac{b_0 + b_1 Z^{-1} + b_2 Z^{-2} + b_3 Z^{-3} + b_4 Z^{-4} + b_5 Z^{-5}}{1 - a_0 Z^{-1} - a_1 Z^{-2} - a_2 Z^{-3} - a_3 Z^{-4} - a_4 Z^{-5}} \quad (4)$$

Where:

- b_0, b_1, b_2, b_3, b_4, b_5: Numerator coefficients
- a_0, a_1, a_2, a_3, a_4, a_5: Denominator coefficients
- Z^{-1}, Z^{-2}, Z^{-3}, Z^{-4}, Z^{-5}: Time delays

Table 2. Numerator coefficients of the filter

b_0	b_1	b_2	b_3	b_4	b_5
5.9796×10^{-5}	2.9898×10^{-4}	5.9796×10^{-4}	5.9796×10^{-4}	2.9898×10^{-4}	5.9796×10^{-5}

Table 3. Denominator coefficients of the filter

a_0	a_1	a_2	a_3	a_4
–3.9845	6.4349	–5.2536	2.1651	–0.3599

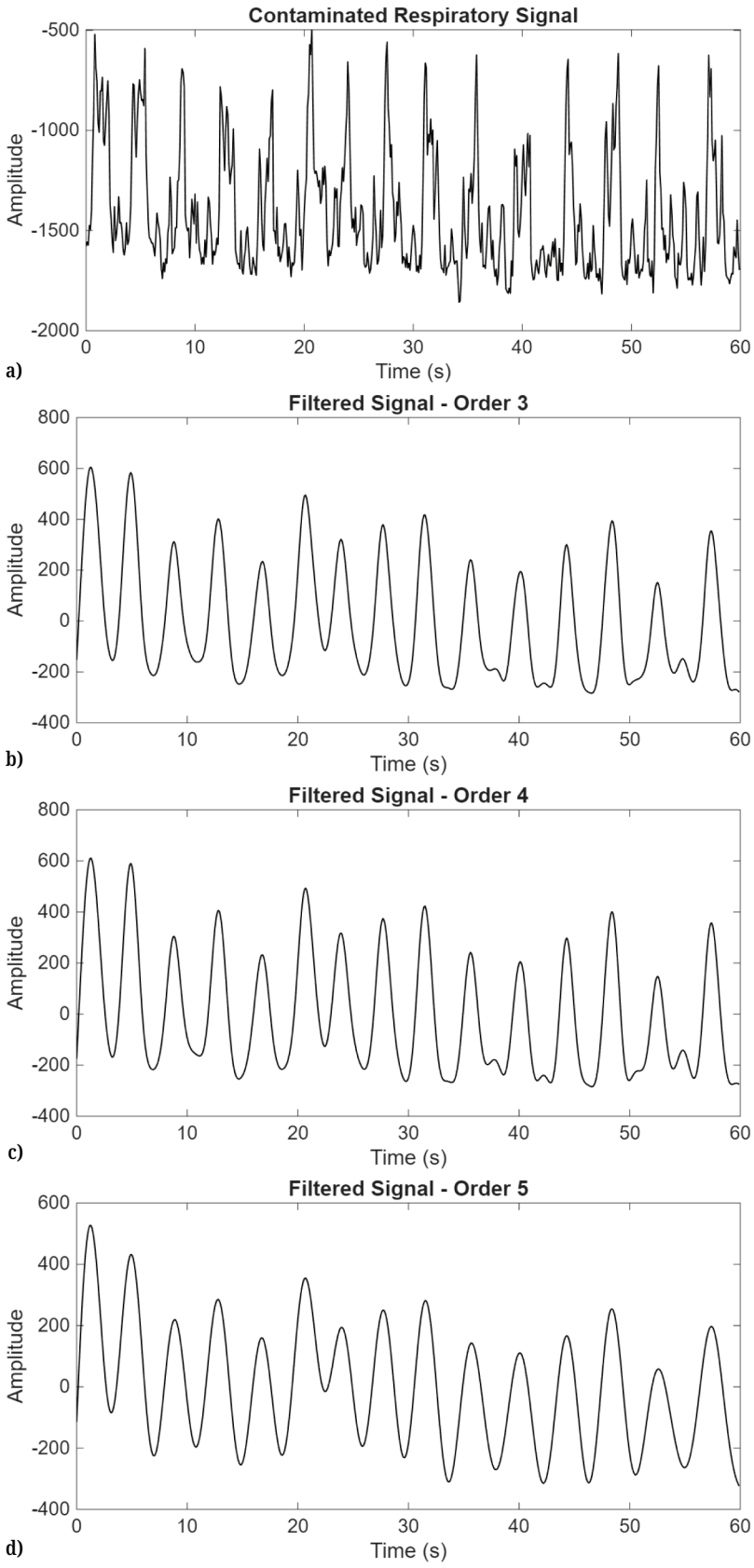

Fig. 7. Comparison of filtered signals: (a) original contaminated signal, (b) filtered signal - 3rd order, (c) filtered signal – 4th order, (d) filtered signal – 5th order

The filtering process was implemented through the difference equation, which for this case is expressed as Equation 5:

$$\begin{aligned} x_1(n) = {} & b_0 \times x(n) + b_1 \times x(n-1) + b_2 \times x(n-2) + b_3 \times x(n-3) \\ & + b_4 \times x(n-4) + b_5 \times x(n-5) + a_0 \times x_1(n-1) \\ & + a_1 \times x_1(n-2) + a_2 \times x_1(n-3) + a_3 \times x_1(n-4) \\ & + a_4 \times x_1(n-5) \end{aligned} \tag{5}$$

Figure 8 illustrates the filtering effect on a respiratory signal acquired during a volunteer's walking. Figure 8a shows the original signal, showing severe contamination from motion artefacts, such as abrupt oscillations and high-frequency pulses that completely mask the underlying respiratory pattern. Figure 8b displays the signal processed using a fifth-order low-pass Butterworth filter implemented in an uncorrected phase configuration. This result demonstrates effective attenuation of the high-frequency components associated with movement, allowing recovery of the characteristic respiratory cycle morphology. However, after filtering, a temporal phase shift between the original and filtered signals is evident, particularly at the inspiration and expiration peaks, which is a direct consequence of the non-linear phase introduced by the filter.

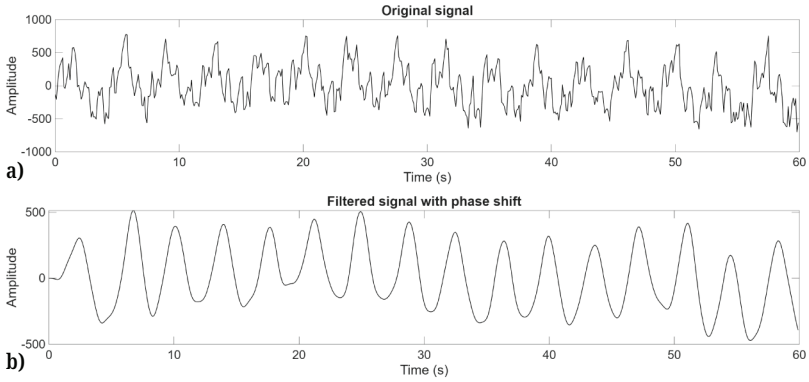

Fig. 8. Comparison between original and filtered signal with phase shift: (a) original contaminated signal, (b) filtered signal with phase shift

To address this, the signal is reversed, the same filter as in the previous case is applied again, and then the signal is reversed once more (see Equations 6, 7, and 8). This compensation for time shifts is necessary because RR calculation requires precise temporal positioning of peaks. The reversal and filtering process can be expressed through the following equations:

$$x_2(n) = x_1(-n) \tag{6}$$

$$\begin{aligned} x_3(n) = {} & b_0 \times x_2(n) + b_1 \times x_2(n-1) + b_2 \times x_2(n-2) + b_3 \\ & \times x_2(n-3) + b_4 \times x_2(n-4) + b_5 \times x_2(n-5) + a_0 \\ & \times x_2(n-1) + a_1 \times x_2(n-2) + a_2 \times x_2(n-3) + a_3 \\ & \times x_2(n-4) + a_4 \times x_2(n-5) \end{aligned} \tag{7}$$

$$x_4(n) = x_3(-n) \tag{8}$$

Figure 9 presents a comparative analysis of respiratory signals processed with a fifth-order low-pass Butterworth filter, highlighting the fundamental differences between conventional unidirectional filtering and bidirectional processing. Figure 9a illustrates how the traditional method introduces a clear temporal phase shift in the respiratory events. In contrast, Figure 9b demonstrates that the bidirectional filtering technique completely preserves the original temporal position of each signal component. This implementation not only maintains effective noise suppression and the characteristic respiratory morphology but also restores precise temporal alignment between the inspiratory/expiratory events and the original recording.

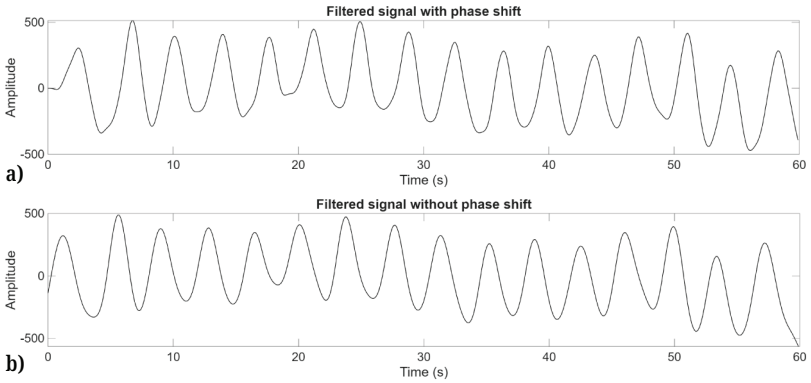

Fig. 9. Comparison between filtered signal with and without phase shift: (a) filtered signal with phase shift, (b) filtered signal without phase shift

Peak detection and RR estimation. The diagram illustrates the final processing stage, where the pre-processed signal is translated into a numerical RR value. Using a peak detection algorithm, the maximum points of each respiratory cycle are identified, and the temporal differences between them are calculated. From these intervals, the RR is mathematically determined and expressed in breaths per minute (bpm), with the final result displayed on the corresponding interface, as shown in Figure 10.

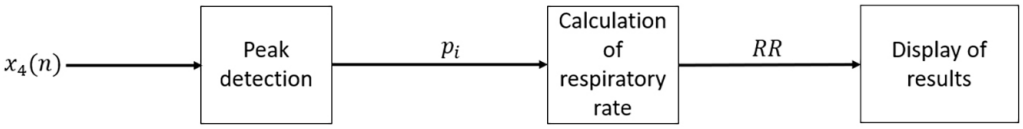

Fig. 10. RR estimation and visualisation diagram

To estimate the RR from the signal, a peak detection algorithm that returns a vector of local maxima (peaks) from the input signal vector is used [18] (see Figure 11). The RR is calculated using the temporal positions of the peaks returned by the algorithm through Equations 9 and 10.

$$M = \frac{1}{S}\sum_{i=1}^{N-1} p_{i+1} - p_i \tag{9}$$

$$RR = \frac{60}{M} bpm \tag{10}$$

Where:

- M: Mean of the summation of differences between peak time positions
- RR: Respiratory rate

- S: Size of the peak vector
- p_i: Time position of a peak

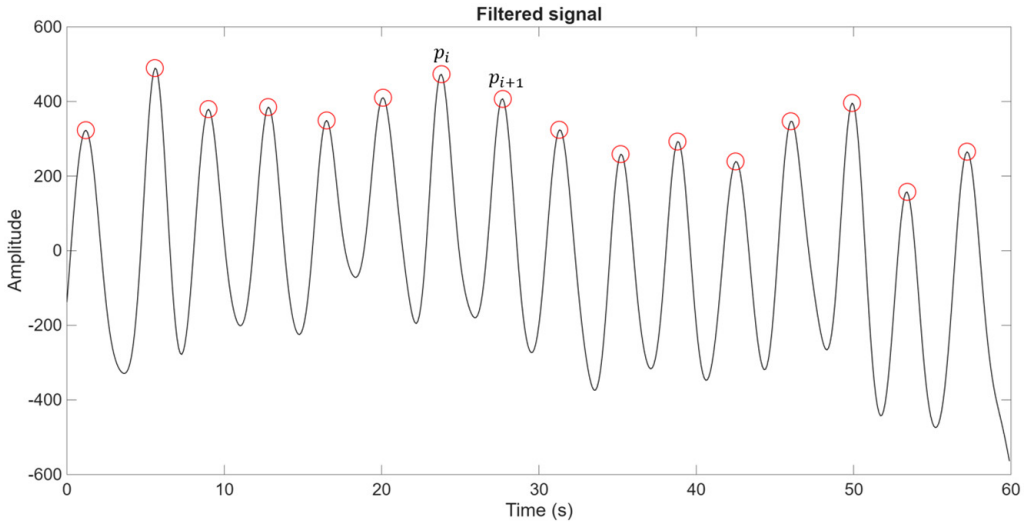

Fig. 11. Positioning of peaks in the filtered signal

Operation and configuration of the proposed IoT device. A mobile application was developed allowing users to monitor RR in real time. The application includes a plot of the original signal which updates every 100 ms, a plot of the filtered signal which updates at each user-defined block time, and a plot of RR over time, as shown in Figure 12.

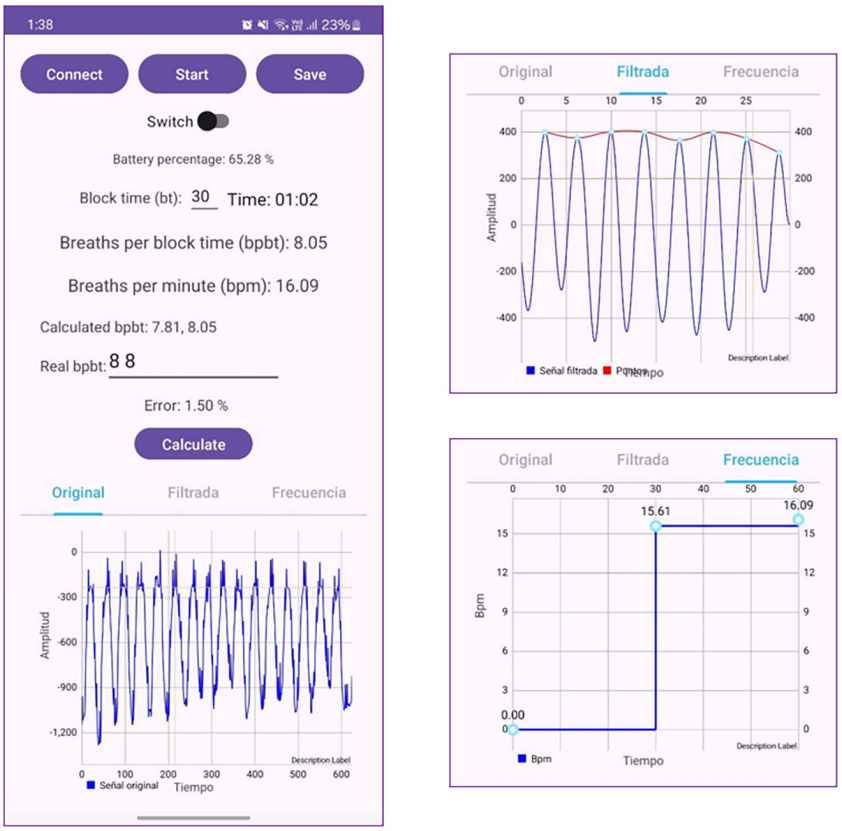

Fig. 12. Mobile application for RR monitoring

For calibration, the sensor was secured around the thorax using an adjustable strap, positioning it over the region of maximum respiratory deformation. Once the device was paired with the mobile application, the presence of a clear breathing waveform was verified; if not, the placement was readjusted until an optimal signal was achieved. Subsequently, the connection mode (Bluetooth or MQTT) was configured, and the analysis block time was set, with a default value of 60 seconds.

During monitoring, the application sampled sensor data every 100 ms and displayed in real time the raw signal, the filtered signal, and the computed respiratory rate. The RR was obtained using a peak-detection algorithm that identifies local maxima in the filtered waveform and determines RR in breaths per minute by applying Equations 9 and 10, which rely on the average time intervals between consecutive peaks.

For validation, the percentage error was used as the evaluation metric by comparing the device's estimated RR with manual stopwatch counts. Tests were conducted under three conditions—rest, moderate motion (~3 km/h), and accelerated motion (~13 km/h)—with data recorded in the application and average error computed according to Equation 12. This procedure enabled a comprehensive assessment of the system's accuracy under realistic usage conditions.

Validation method. The percentage error, obtained from Equation 11, is used as the accuracy metric:

$$\%E = \left| \frac{RR_{prototype} - RR_{GoldStandar}}{RR_{GoldStandar}} \right| \times 100\% \tag{11}$$

Where:

- $RR_{prototype}$: RR from the prototype.
- $RR_{GoldStandar}$: RR manually measured with a stopwatch.
- $\%E$: Percentage error.

The percentage error validation method provides a relative measure of error compared to the true value. A result different from zero indicates a discrepancy between the estimate and the true value. A percentage error of zero signifies an exact match between the estimate and the true value.

The average percentage error across different scenarios is calculated using Equation 12:

$$\%E_p = \frac{1}{L} \sum_{i=1}^{L} \%E_i \tag{12}$$

Where:

- $\%E_p$: Average percentage error.
- $\%E_i$: Percentage error for a single test.
- L: Number of tests.

The study was conducted in the Structure, Function, and Procedure Laboratory of the School of Medicine at the Peruvian University of Applied Sciences, with the voluntary participation of healthy athletes. In accordance with institutional policies for academic projects involving non-invasive procedures, formal approval from an ethics committee was not required, as this phase focused exclusively on equipment performance and accuracy verification. Nevertheless, in a subsequent stage of the project, the protocol will be submitted to an ethics committee to initiate the corresponding clinical testing phase.

Following this preparatory stage, the device validation was performed across three scenarios: rest, moderate motion, and accelerated motion. To ensure comparability, data acquisition was carried out simultaneously using both the proposed IoT device and the manual reference method. At the start of each test, a stopwatch was activated as the volunteer began counting their breaths, while the device performed its automatic estimation in parallel, ensuring that both recordings covered the same time interval. In the first scenario, the volunteer remained at rest; in the second, they walked at an approximate speed of 3 km/h; and in the third, they ran at a speed close to 13 km/h. During each test, the mobile application displayed in real time the raw signal, the filtered signal, and the RR calculated through the peak-detection algorithm, applying Equations 9 and 10. Subsequently, the results obtained from the device were compared with the manual count, and the average percentage error was computed according to Equation 12, thereby enabling a comprehensive evaluation of the system's accuracy under realistic usage conditions.

4 RESULTS AND DISCUSSION

This section describes the results obtained during the three validation scenarios of the respiratory monitoring system, along with their respective analyses. The performance of the device under rest and motion conditions is presented, comparing the measurements with reference values obtained via a stopwatch. The results demonstrate the effectiveness of the filtering and the high accuracy of the system in all evaluated scenarios, with average errors below 2% even at speeds up to 13 km/h. The results of each experimental scenario are detailed below.

4.1 Validation Scenario 1: Estimation of RR at rest

In Scenario 1, the number of breaths in volunteers standing still was counted and timed with a stopwatch, after which their RR was computed. The results were compared with the proposed device's estimation, and the average percentage error was calculated as shown in Table 4.

Table 4. Results obtained in Scenario 1

Volunteer	Test 1		Test 2		Test 3		Avg. Error (%E_p)
	Respiratory Rate (*RR*)		Respiratory Rate (*RR*)		Respiratory Rate (*RR*)		
	Device	Stopwatch	Device	Stopwatch	Device	Stopwatch	
1	13.66	14	14.23	14	18.65	19	1.97%
2	10.29	10	11.32	11	17.33	17	2.54%
3	13.8	14	15.5	15	14.2	14	2.02%
4	14.21	14	13.83	14	14.28	14	1.56%
5	14.18	14	14.96	15	15.1	15	0.74%
6	27.38	28	22.94	23	19.69	20	1.35%
7	21.22	21	21.3	21	22.88	22	2.10%
8	16.43	16	15.41	15	15.51	15	2.88%
9	13.66	14	14.23	14	18.65	19	1.97%
10	12.95	13	21.24	22	19.91	20	1.47%

Discussion: The results obtained in the resting scenario (Table 4) show an average error of 1.86%, confirming the device's high accuracy under static conditions. This performance can be attributed to the absence of motion artefacts, which allows the respiratory signal to preserve a well-defined morphology and facilitates peak detection following Butterworth filtering. Compared with systems based on BioZ or piezoresistive sensors—which typically report errors between 1% and 3% at rest [4]—the proposed device demonstrates competitive performance without requiring direct skin contact, thereby reducing issues related to perspiration and enhancing user comfort. Nevertheless, intersubject variability was observed in volunteers with elevated respiratory rates (>25 breaths per minute), indicating that proper initial calibration and the magnet–sensor distance are critical factors for maintaining accuracy.

4.2 Validation Scenario 2: Estimation of RR during motion at an approximate speed of 3 km/h

In Scenario 2, volunteers moving 5 metres at close to 3 km/h had their number of breaths counted and timed with a stopwatch, after which their RR was computed. The results were compared with the proposed device's estimation, and the percentage error was calculated as shown in Table 5.

Table 5. Results obtained in Scenario 2

Volunteer	Test 1		Test 2		Test 3		Avg. Error (%E_p)
	Respiratory Rate (*RR*)		Respiratory Rate (*RR*)		Respiratory Rate (*RR*)		
	Device	Stopwatch	Device	Stopwatch	Device	Stopwatch	
1	16.87	17	19.96	20	19.64	19	1.41%
2	22.43	23	18.5	18	17.68	18	2.33%
3	19.97	20	17.9	18	16.42	16	1.09%
4	16.54	16.5	18.41	18.5	15.5	15.5	0.24%
5	20.73	21	19.12	19	16.07	16	0.78%
6	16.48	16	14.66	15	11.83	12	2.25%
7	10.97	11	14.67	14	10.97	11	1.70%
8	15.76	16	13.09	13	15.48	15	1.76%
9	14.09	14	15.36	15	14.88	15	1.26%
10	15.75	16	16.25	16	15.94	16	1.16%

Discussion: Under moderate motion, the average error was 1.4% (refer to Table 5), demonstrating the robustness of the filtering strategy against kinematic artefacts. This result is noteworthy, as previous studies using stretchable sensors have reported errors exceeding 4% at comparable walking speeds [3]. The architecture based on triaxial magnetometry combined with bidirectional filtering preserved the temporal alignment of respiratory cycles, a key requirement for accurately computing the RR. Nevertheless, increased variability was observed in volunteers with irregular breathing patterns during walking, indicating the need for adaptive algorithms capable of adjusting the cutoff frequency in real time.

4.3 Validation Scenario 3: Estimation of RR during motion at an approximate speed of 13 km/h

Finally, for Scenario 3, and similarly to the previous scenarios, volunteers had their breaths counted and timed while moving close to 13 km/h, and their respiratory rates were calculated. The results were compared with the proposed device's estimation, and the percentage error was calculated as shown in Table 6.

Table 6. Results obtained in Scenario 3

Volunteer	Test 1		Test 2		Test 3		Avg. Error (%E_p)
	Respiratory Rate (*RR*)		Respiratory Rate (*RR*)		Respiratory Rate (*RR*)		
	Device	Stopwatch	Device	Stopwatch	Device	Stopwatch	
1	27.23	27	28.88	28	26.09	26	1.41%
2	17.61	18	16.01	16	16.1	16	0.95%
3	19.97	20	19.32	19	20.79	20	1.87%
4	20.8	20	19.64	19	18.96	19	2.49%
5	18.47	19	20.61	21	19.28	19	2.04%
6	15.05	15	16.87	16	15.29	15	2.46%
7	25.61	26	23.41	23	22.56	23	1.73%
8	19.79	20	23.42	23	21.25	21	1.34%
9	18.99	19	18.25	18	17.95	18	0.57%
10	22.43	23	18.85	19	19.15	19	1.35%

Discussion: Under high-mobility conditions, the device maintained an average error of 1.62% (Table 6), substantially outperforming the limitations reported in the state of the art, where errors of up to 14% have been documented at speeds as low as 6 km/h [3]. This finding supports the hypothesis that Z-axis measurement combined with 5th-order Butterworth filtering constitutes an effective strategy for mitigating motion-induced noise. Nonetheless, it is recognised that the fixed cutoff frequency (0.5 Hz) could attenuate respiratory components in subjects exhibiting hyperventilation (>40 bpm), suggesting that future iterations should explore adaptive filters or adjustable passbands. The ability to maintain high precision in this scenario opens opportunities for applications in high-performance sports and ambulatory monitoring of active patients.

4.4 Comparison with the state of the art

The developed device significantly surpasses the state of the art in scenarios demanding high mobility without sacrificing precision (refer to Table 7), a critical factor for applications in sports health or ambulatory patient monitoring. While existing systems prioritise precision at low speeds (e.g., 1.4% at 6 km/h) or sacrifice accuracy to operate in limited dynamic ranges (e.g., 14% error), this proposal seeks to balance innovation and applicability and has been validated under conditions representative of real-world use.

Table 7. Comparison with the state of the art

Reference	Speed	Avg. Error (%E_p)
Proposed IoT Device	13 km/h	1.62%
Monitoring respiratory rates with a wearable system using a stretchable strain sensor during moderate exercise [4]	6 km/h	14%
Wireless wearable ultrasound sensor on a paper substrate to characterise respiratory behaviour [3]	7.2 km/h	4.25%
A Wearable BioZ Chest Patch for Real-Time Ambulatory Respiratory Monitoring [10]	6 km/h	1.4%

Table 7 summarises the comparison between the proposed IoT device and the main solutions reported in the literature. Our system maintains an average error of 1.62% even at a speed of 13 km/h, representing a critical scenario not addressed by most existing technologies. For instance, [4] reports a 14% error at 6 km/h when using stretchable sensors, whose accuracy degrades significantly in the presence of sudden movements and perspiration. Similarly, [3] describes ultrasound-based systems that restrict their operation to speeds below 7.2 km/h, with errors exceeding 4% [3]. Although chest patches based on BioZ demonstrate competitive performance (≈1.4% at 6 km/h) [10], they rely on intimate skin contact, which limits their applicability in scenarios involving intense sweating or prolonged exercise.

In this context, the superiority of the proposed device can be attributed to three key factors: (i) the use of triaxial magnetometry to measure Z-axis displacement, which reduces dependence on direct skin contact and minimises sensitivity to moisture; (ii) the implementation of a 5th-order low-pass Butterworth filter with bidirectional processing, which effectively suppresses motion artefacts without introducing temporal phase shifts; and (iii) a dual communication architecture (Bluetooth + Wi-Fi), which enables both local and remote real-time monitoring—a capability not present in several commercial solutions.

Consequently, these advantages position the device as a robust alternative for applications in high-performance sports, telemedicine, and ambulatory monitoring, where mobility cannot be compromised in favour of precision. However, it is acknowledged that the limited sample size and the absence of testing in clinical populations are constraints that should be addressed in future studies. Moreover, the fixed cutoff frequency (0.5 Hz) may restrict detection in subjects exhibiting hyperventilation (>40 breaths per minute), indicating that future work should explore adaptive filters and machine-learning-based algorithms to improve scalability and enhance the detection of respiratory anomalies.

5 CONCLUSIONS

This study successfully developed and validated a novel wireless IoT device for accurate RR monitoring during physical activity. The system's efficacy is rooted in the strategic use of a triaxial magnetic sensor, where the Z-axis was identified as providing the most reliable signal due to its superior integrity and lower susceptibility to motion-induced noise compared to the other axes. A critical factor in achieving high precision was the implementation of a bidirectional, fifth-order low-pass Butterworth filter, which effectively suppressed motion artefacts while preserving the respiratory waveform's morphology and eliminating phase distortion. Rigorous

validation under conditions ranging from rest to high-speed motion (13 km/h) demonstrated the device's exceptional performance, with an average error consistently below 2%, surpassing existing solutions in high-mobility scenarios.

Key practical insights for optimal operation include maintaining a magnet-sensor distance of approximately 2.2 cm and employing an adjustable elastic strap to maximise signal sensitivity by ensuring consistent chest contact. A preliminary calibration is also recommended to account for variations in user physique. The proposed platform establishes a strong foundation for future research, with promising directions including the integration of machine learning algorithms for real-time anomaly detection, such as sleep apnoea, and further exploration of the system's scalability at even higher speeds while maintaining clinical-grade accuracy.

6 REFERENCES

[1] A. Nicolò, C. Massaroni, E. Schena, and M. Sacchetti, "The importance of respiratory rate monitoring: From healthcare to sport and exercise," *Sensors*, vol. 20, no. 21, p. 6396, 2020. https://doi.org/10.3390/s20216396

[2] G. Kemper, A. Oshita, R. Parra, and C. Herrera, "PE20231412Z: Equipo electrónico portátil orientado al monitoreo de la respiración nasal y bucal a través de la extracción de características de señales acústicas," *Patent PE20231412Z*, 2023. Accessed: Sep. 22, 2025. [Online]. Available: https://worldwide.espacenet.com/patent/search/family/088790835/publication/PE20231412Z?q=pn%3DPE20231412Z

[3] A. Chen *et al.*, "Wireless wearable ultrasound sensor on a paper substrate to characterize respiratory behavior," *ACS Sensors*, vol. 4, no. 4, pp. 944–952, 2019. https://doi.org/10.1021/acssensors.9b00043

[4] A. Yamamoto *et al.*, "Monitoring respiratory rates with a wearable system using a stretchable strain sensor during moderate exercise," *Medical & Biological Engineering & Computing*, vol. 57, no. 12, pp. 2741–2756, 2019. https://doi.org/10.1007/s11517-019-02062-2

[5] A. Al-Halhouli *et al.*, "Screen-printed wearable sensors for continuous respiratory rate monitoring: Fabrication, clinical evaluation, and point-of-care potential," *Materials Advances*, vol. 5, no. 24, pp. 9586–9595, 2024. https://doi.org/10.1039/D4MA00510D

[6] Z. Yin, Y. Yang, C. Hu, J. Li, B. Qin, and X. Yang, "Wearable respiratory sensors for health monitoring," *NPG Asia Mater*, vol. 16, no. 8, 2024. https://doi.org/10.1038/s41427-023-00513-9

[7] Hexoskin, "Hexoskin Smart Shirt—Connected Health Platform," *Carré Technologies Inc.*, 2025. [Online]. Available: https://hexoskin.com [Accessed: Dec. 10, 2025].

[8] RTMsense, "RTMsense Respiratory Monitoring System – RTM Vital Signs," 2025. Accessed: Nov. 22, 2025. [Online]. Available: https://rtmvitalsigns.com/products/rtmsense-respiratory-monitoring-system

[9] D. Kim, J. Lee, M. K. Park, and S. H. Ko, "Recent developments in wearable breath sensors for healthcare monitoring," *Communications Materials*, vol. 5, p. 41, 2024. https://doi.org/10.1038/s43246-024-00480-w

[10] C. Qiu, F. Wu, W. Han, and M. R. Yuce, "A wearable bioimpedance chest patch for real-time ambulatory respiratory monitoring," *IEEE Transactions on Biomedical Engineering*, vol. 69, no. 9, pp. 2970–2981, 2022. https://doi.org/10.1109/TBME.2022.3158544

[11] M. Jurado, B. Palma, A. Figueroa, and G, Kemper, "An IoT monitoring system based on artificial intelligence image recognition and EMG signal processing for abdominal exercise performance," *International Journal of Online and Biomedical Engineering (iJOE)*, vol. 21, no. 3, pp. 116–141, 2025. https://doi.org/10.3991/ijoe.v21i03.52305

[12] Espressif Systems, "Get Started – ESP32—ESP-IDF Programming Guide (latest documentation)," 2016. Accessed: July 20, 2025. [Online]. Available: https://docs.espressif.com/projects/esp-idf/en/latest/esp32/get-started/index.html

[13] QST, "QMC5883L | Datasheet | QST | LCSC Electronics," 2016. Accessed: July 20, 2025. [Online]. Available: https://lcsc.com/datasheet/lcsc_datasheet_2410121532_QST-QMC5883L_C976032.pdf

[14] Allelco Electronics, "MAX17043/MAX17044 Li+ Battery: Specifications, Pinout, and Datasheet," n.d. Accessed: July 20, 2025. [Online]. Available: https://www.allelcoelec.com/blog/MAX17043-MAX17044-Li-Battery-Specifications,Pinout,and-Datasheet.html

[15] Torex Semiconductor Ltd., "XC6220 Series 1A LDO voltage regulator with 'Green Operation'," *Datasheet*, 2010. [Online]. Available: https://product.torexsemi.com/system/files/series/xc6220.pdf [Accessed: July 20, 2025].

[16] L. Puente Maestu, M. C. Juárez Morales, and e. Ojeda Castillejo, "Prueba de ejercicio cardio-respiratorio progresivo," monografía, Neumomadrid, 2013. [Online]. Available: https://www.neumomadrid.org/wp-content/uploads/monogxviii_11._prueba_de_ejercicio.pdf [Accessed: Dec. 10, 2025].

[17] Great Magtech, "El sorprendente imán de neodimio: una guía completa – Conocimiento," 2023. Accessed: Sep. 15, 2024. [Online]. Available: https://es.greatmagtech.com/info/the-amazing-neodymium-magnet-a-complete-guide-83347347.html

[18] MathWorks, "Find local maxima – MATLAB findpeaks," 2024. Accessed: June 01, 2024. [Online]. Available: https://la.mathworks.com/help/signal/ref/findpeaks.html?lang=en

7 AUTHORS

Jhosep Ccoanqui is with the Faculty of Engineering, School of Electronic Engineering, Universidad Peruana de Ciencias Aplicadas, Av. Prolongación Primavera 2390, Monterrico, Santiago de Surco, Lima 15023, Peru.

Eros Huamani is with the Faculty of Engineering, School of Electronic Engineering, Universidad Peruana de Ciencias Aplicadas, Av. Prolongación Primavera 2390, Monterrico, Santiago de Surco, Lima 15023, Peru.

Guillermo Kemper is with the Faculty of Engineering, School of Electronic Engineering, Universidad Peruana de Ciencias Aplicadas, Av. Prolongación Primavera 2390, Monterrico, Santiago de Surco, Lima 15023, Peru (E-mail: guillermo.kemper@upc.pe).